

## MEASURING THE BULK LORENTZ FACTORS OF GAMMA-RAY BURSTS WITH *FERMI*

QING-WEN TANG<sup>1,2</sup>, FANG-KUN PENG<sup>1,2</sup>, XIANG-YU WANG<sup>1,2</sup>, PAK-HIN THOMAS TAM<sup>3</sup>

<sup>1</sup> School of Astronomy and Space Science, Nanjing University, Nanjing 210093, China; xywang@nju.edu.cn

<sup>2</sup> Key laboratory of Modern Astronomy and Astrophysics (Nanjing University), Ministry of Education, Nanjing 210093, China

<sup>3</sup> Institute of Astronomy and Space Science, Sun Yat-Sen University, Guangzhou 510275, China; tanbxuan@mail.sysu.edu.cn

*Draft version June 9, 2021*

### ABSTRACT

Gamma-ray bursts (GRBs) are powered by ultra-relativistic jets. Usually a minimum value of the Lorentz factor of the relativistic bulk motion is obtained based on the argument that the observed high energy photons ( $\gg$  MeV) can escape without suffering from absorption due to pair production. The exact value, rather than a lower limit, of the Lorentz factor can be obtained if the spectral cutoff due to such absorption is detected. With the good spectral coverage of the Large Area Telescope (LAT) on *Fermi*, measurements of such cutoff become possible, and two cases (GRB 090926A and GRB 100724B) have been reported to have high-energy cutoffs or breaks. We systematically search for such high energy spectral cutoffs/breaks from the LAT and the Gamma-ray burst monitor (GBM) observations of the prompt emission of GRBs detected since August 2011. Six more GRBs are found to have cutoff-like spectral feature at energies of  $\sim 10 - 500$  MeV. Assuming that these cutoffs are caused by pair-production absorption within the source, the bulk Lorentz factors of these GRBs are obtained. We further find that the Lorentz factors are correlated with the isotropic gamma-ray luminosity of the bursts, indicating that more powerful GRB jets move faster.

*Subject headings:* gamma rays bursts: general—method: data analysis—radiation mechanism: non-thermal

### 1. INTRODUCTION

Gamma-Ray Bursts (GRBs) are the most energetic transient phenomena in the universe. The initial brief and intense gamma-ray flash, the so-called prompt emission, is thought to be produced in an ultra-relativistic outflow, as argued by the fact that high energy photons ( $\gg$  MeV) escape out of the source without suffering from absorption due to pair production ( $\gamma\gamma \leftrightarrow e^+e^-$ ) (e.g. Krolik& Pier (1991); Fenimore et al. (1993); Woods& Loeb (1995); Baring& Harding (1997)). Requiring that the absorption optical depth  $\tau_{\gamma\gamma} \lesssim 1$  for high energy photons, one can deduce a lower limit on the bulk Lorentz factor ( $\Gamma$ ) of the emitting region, which is usually  $\gtrsim 100$  (Lithwick& Sari 2001).

The absorption should cause a spectral cutoff or break in the highest energy end, which is expected to be seen within fireball shock model if the energy coverage and sensitivity of the detector is sufficiently good. With the greatly increased spectral coverage of the Large Area Telescope (LAT) on *Fermi*, search for such high energy spectral cutoff/break becomes possible. A spectral break around 0.4 GeV is detected for the first time in GRB 090926A (Ackermann et al. 2011). In the first *Fermi*/LAT GRB catalog (Ackermann et al. 2013), which summarized the spectral analysis of all LAT-detected GRBs up to July 2011, one more GRB (i.e. GRB 100724B) is reported to have a spectral cutoff at the highest energy end. In this paper, we perform a thorough analysis of GRBs detected by *Fermi*-LAT between August 1, 2011 and October 30, 2014 to search for cutoff-like spectral features. In §2, we present the sample selection (§2.1), data reduction (§2.2) and the results (§2.3). We find six out of twenty-eight GRBs showing cutoff-like features, and the rest bursts can be adequately modeled by the Band function. In §3, assuming the cutoffs are caused by the pair-production absorption in emission region, the bulk Lorentz factors ( $\Gamma$ ) are obtained (§3.1). With the total eight GRBs having measurements of the Lorentz factors,

we further test the  $\Gamma - L_{\gamma, \text{iso}}$  and  $\Gamma - E_{\gamma, \text{iso}}$  correlations (§3.2). Then we give a summary (§3.3). Throughout this paper, we adopt a Hubble constant  $H_0 = 71 \text{ km s}^{-1} \text{ Mpc}^{-1}$ ,  $\Omega_M = 0.27$  and  $\Omega_\Lambda = 0.73$ .

### 2. DATA ANALYSIS AND RESULTS

#### 2.1. The burst sample

Since the launch of *Fermi* satellite,  $\sim 250$  GRBs per year are detected with GBM. When sources are bright enough, the spacecraft will slew to the location of the burst and performs a pointed observation autonomously. So the prompt emission of some GRBs were simultaneously observed with LAT. We search for such GRBs to make joint spectral analysis. A total of 49 GRBs are detected by the *Fermi*/LAT between August 1, 2011 and October 31, 2014, as listed in the LAT Burst Online Catalog<sup>1</sup>. Focusing on the prompt phase, 28 of them were reported by the *Fermi*/LAT collaboration (through GCN circulars) to have LAT detection ( $>100$  MeV) during the main gamma-ray emission phase, i.e., the time interval of GBM data analysis. Table 1 shows the information of these 28 GRBs, including the position derived from the LAT photons, the burst time interval used by the GBM team for spectral analysis (which is also the time interval used in our joint GBM/LAT analysis) and the LAT boresight angle at the GBM trigger time.

#### 2.2. Data analysis

##### 2.2.1. Data preparation and event selection

We extract both LAT and GBM data from the FSSC (Fermi Science Support Center). During the spectral analysis, the Time-Tagged Events (TTE), as well as CTIME, data files from two or three NaI detectors and one BGO detector were used. For 15 out of the 28 GRBs, publicly LAT Low-Energy (LLE)

<sup>1</sup> <http://fermi.gsfc.nasa.gov/ssc/observations/types/grbs/lat/>

data are also available, as shown in Table 1. We then performed joint spectral analysis including LLE data for these 15 bursts. For each NaI detector, channels below 8 keV or above 1000 keV are ignored. For BGO, we do not include channels below 250 keV or above 40 MeV. The time interval for spectral analysis is GBM  $T_{90}$ , which contains the emission from 5% of its total fluence to 95% (Table 1) (Paciesas et al. 2012; Goldstein et al. 2012; von Kienlin et al. 2014; Gruber et al. 2014). The joint spectral fitting of GBM/LAT data is performed with RMFIT version 4.3.2., which judge the goodness of fit using the Castor Statistic (CSTAT) to handle correctly the small number of events at the high energy.

### 2.2.2. Background estimation and spectrum extraction

1) GBM data. For each detector, two off-pulse time intervals (one before and one after the GRB prompt pulses) are selected, and then we fit them with polynomial functions in RMFIT. The order of the fitting polynomial was chosen as one in the beginning, incremented by one each time, until we get a reduced  $\chi^2 \simeq 1$ , with a maximum of four. In order to minimize the statistical and systematic uncertainties (and hence ensure a reliable background estimate), the off-pulse time intervals must be close to the burst interval, have a long enough duration, and do not contain bumps or other structures in the light curve. After each fit, we check visually that the residual are consistent with the statistical fluctuations. If not, we repeat the procedure by changing the choice for the off-pulse intervals. The CTIME event data are employed to obtain background models.

2) LLE data. The LLE data products are delivered by the LAT team to the FSSC and to the public which provides large effective area at low energies of the LAT detector, joining the LAT and GBM energy ranges. We include the LLE events from 30 MeV to 130 MeV in the fit, similar to Axelsson et al. (2012). We estimate its background using the same procedure as GBM data but with the publicly LLE spectrum products which can be used in RMFIT and XSPEC.

3) LAT data ( $>100$  MeV). We derive the LAT spectrum files and response files using the *Fermi* Science Tools package, version v9r32p5<sup>2</sup>. We select transient-class events from LAT observations, and instrument response functions (IRFs) P7REP\_TRANSIENT\_V15 are used. We excluded the events with zenith angles  $>100^\circ$  in order to avoid a significant contribution of Earth-limb gamma-rays using the tool *gtselect*. All events in a region of interest (ROI) of  $12^\circ$  around the positions (see Table. 1) of burst are used. LAT spectra are divided into 20 logarithmically spaced energy bins from 100 MeV to 10 GeV. The spectrum and the response matrix of each GRB are derived using *gtbin* and *gtrspgen*. Background of LAT spectra are calculated by the BKG script with a constant ROI by adding a command of "*ROI\_Calculate=0*" (Vasileiou 2013).

### 2.2.3. Spectral models

GRB time-integrated spectra are usually fitted with a smoothed broken power law function, the so-called "Band function" (Band et al. 1993). Possible superposition of a thermal component on the nonthermal spectrum was claimed in *BATSE* and *Fermi* GRBs (Guiriec et al. 2011, 2013, 2015; Preece et al. 2014; Ryde & Pe'er 2009; Ryde 2005; Ryde et al.

2010, 2011; Pe'er et al. 2012; Yu et al. 2015). Other non-Band models, such as synchrotron model (Burgess et al. 2011, 2014; Preece et al. 2014), are also proposed. We do not include the thermal emission in the analysis, because the thermal emission with a single temperature is usually found in the careful time-resolved analysis, while our searching for LAT spectral cutoff needs to be done in the time-integrated spectrum in order to have enough LAT photons. Furthermore, we also find that, when a thermal component can be adequately added in a time-integrated GRB spectrum, the LAT cutoff energy remains unchanged (although it changes the peak energy of the Band component). For some non-Band models, such as the Power-law (PL), smoothly broken power law model (SBPL), Comptonized model (Comp) (Goldstein et al. 2012; Gruber et al. 2014), we found that they do not improve the fit over the Band model significantly for the bursts in our sample. For these reasons, and considering that Band model is a widely used phenomenological model, we use the Band model as the primary model in our analysis<sup>3</sup>. Meanwhile an extra power-law component (sometimes with high energy cutoff) was also found in some LAT-detected GRBs, such as GRB 090902B, GRB 090510, and GRB 090926A (Abdo et al. 2009a; Ackermann et al. 2010, 2011).

Thus, we assume the Band function or the Band plus a power-law function for the fundamental GRB spectral models. To search for cutoff-like features at the high-energy end, three spectral models are considered, i.e.,

(a) Band model, that is

$$N_{Band} = B(E) = A \begin{cases} (E/100\text{keV})^\alpha e^{-(2+\alpha)/E_p} & \text{if } E < E_b \\ [(\alpha - \beta)E_p / (100\text{keV}(2 + \alpha))]^{(\alpha - \beta)} \\ e^{\beta - \alpha} (E/100\text{keV})^\beta & \text{if } E \geq E_b \end{cases}$$

where  $E_b = (\alpha - \beta)E_p / (2 + \alpha)$ ,  $\alpha$  is the photon index at low energy,  $\beta$  is the photon index at high energy and  $E_p$  is the peak energy in the  $E^2 B(E)$  representation.

(b) BandCut model, the Band function with an exponential cutoff:

$$N_{BandCut} = B(E) e^{-E/E_c},$$

where  $E_c$  is the cutoff energy.

(c) Band+PLcut model, that is the Band function plus a power-law model with an exponential cutoff

$$N_{Band+PLcut} = B(E) + k(E/E_{piv})^\lambda e^{-E/E_c},$$

where  $E_{piv}$  is the pivot energy and  $E_c$  is the cutoff energy.

To take into account the uncertainties caused by inter-calibration between the GBM and the LAT, we allow for an effective area correction during the combined fits. The calibration constant for the LAT is fixed to one and data from other detectors are allowed to vary during the fits (Ackermann et al. 2013). The correction factors typically have values between 0.9 and 1.1 for the NaI detectors and between 0.7 and 1.3 for the BGO detectors.

We employ the following three criteria to determine the preferred spectral model: (1) the goodness of the fitting, which is measured by the reduced CSTAT (a smaller CSTAT value shows a better fit, and the difference,  $\Delta\text{CSTAT}$ , is

<sup>3</sup> There are 3 out of 28 GBM+LAT GRBs (GRB 090531B, 100728A and 110328B) in the first *Fermi*-LAT GRB catalog (three years data) (Ackermann et al. (2013)), which could be best fitted by a single Comptonized model in the GBM interval ( $T_{90}$ ). But these GRBs would not be detected significantly in the LAT range during  $T_{90}$  with TS smaller than 9.

<sup>2</sup> available at the Fermi Science Support Center (FSSC), <http://fermi.gsfc.nasa.gov/ssc/>

roughly equal to square of significance of improvement, see Ackermann et al. (2011)), here we claim a significant change with  $\Delta\text{CSTAT}$  larger than 28; (2) the robustness of the model parameters, which is measured with the errors of the parameters; (3) whether a structure exists in the residual distribution.

### 2.3. Results

We finally obtain the following results about the joint spectra of *Fermi* LAT GRBs: 22 GRBs are adequately fitted with the Band function and the rest 6 GRBs show high energy cutoff features: an exponential cutoff from the high energy part of Band component or from extra power law component. The observed spectra with our fitting curve are shown in Figure 1 and the results are reported in Table 2-3.

#### 2.3.1. Sample fitted by the Band function

The low energy photon index  $\alpha$  of the sub-sample is in the range of  $-1.1$  to  $-0.3$  with an average value of  $-0.67$  and the standard derivation of  $0.41$ , despite of one GRB with  $\alpha$  larger than  $0$ . The high energy photon index  $\beta$  ranges from  $-3.0$  to  $-2.0$  with an average value of  $-2.62$  and the standard derivation of  $0.33$ . The peak energy  $E_p$  ranges from  $70$  keV to  $900$  keV with an average value of  $499$  keV and the standard derivation of  $387$  keV.

Compared with the recent results of *Fermi*/GBM catalog:  $E_p = 196_{-336}^{+100}$  keV,  $\alpha = -1.08_{-0.43}^{+0.44}$  and  $\beta = -2.14_{-0.27}^{+0.37}$  (Gruber et al. 2014), *Fermi*/LAT GRBs (our sample) have higher peak energy, harder low energy photon index and softer high energy photon index<sup>4</sup>.

#### 2.3.2. Sample with high energy spectral cutoff

Firstly, we reanalyzed the first *Fermi*/LAT GRB catalog (Ackermann et al. 2013). Only two GRBs (i.e., GRB 090926A and 100724) are found to show convincing evidence of spectral cutoffs or breaks. GRB 090926A and 100724B can be modelled, respectively, by the Band+PLCut and BandCut models (see Figure 1). The results are consistent with the results in Ackermann et al. (2013).

Among the 28 LAT GRBs detected since August 2011, 6 GRBs are found to deviate from the Band model with  $\Delta\text{CSTAT} > 28$ : GRB 130504C, GRB 130821A, GRB 131231A, GRB 131108A, GRB 140206B and GRB 141028A. Except for GRB 131108A, BandCut model is the preferred model with  $\Delta\text{CSTAT}$  large than 28, as shown in Table 3. Note that, we perform the spectral analysis of GRB 130821A in the main burst phase, i.e, 3 seconds before and 49 seconds after trigger time (Jenke 2013b). The spectral fits of all the 6 GRBs are shown in Figure 1.

We find that the Band function cannot fit GRB 131108A's spectrum well, as also noted by Giuliani et al. (2014). Following our procedures, its time-integrated spectrum can be fitted by the Band+PLCut model, with a  $\Delta\text{CSTAT}=29.5$  improvement over the Band model. The cutoff energy is found to be at  $347.1 \pm 52.8$  MeV (see Table 3). Giuliani et al. (2014)

<sup>4</sup> GRB 130427A suffers from pile-up and buffer saturation effect. We perform spectral analysis with duration  $\sim 138$  seconds and find that adding a Power law component can improve the CSTAT value significantly (Preece et al. 2014; Ackermann et al. 2014), i.e,  $\Delta\text{CSTAT}=522$ . And at its low energy band there maybe exists a thermal emission component (Preece et al. 2014; Yu et al. 2015). As mentioned above, we don't consider it during our fit. For GRB 140104B, we exclude the events below 50 keV, as its low-energy part cannot be modeled by any of the aforementioned models.

claimed that the Band function plus a smoothly broken power function (SBPL) can fit the data well. We test this model and find that Band+SBPL has a similar CSTAT value as that of Band+PLCut. We adopt Band+PLCut as the preferred model since it contains one less parameter than Band+SBPL.

## 3. IMPLICATIONS AND DISCUSSIONS

Including GRB 090926A and GRB 100724B, there are 8 GRBs showing cutoff-like spectral features in the high-energy emission and the cutoff energy ranges from  $\sim 10$  to several hundred MeV. We note that the cutoffs obtained for the BandCut model cluster around tens of MeV and no cutoff above 100 MeV is seen. This may be because the limited number of photons above 100 MeV does not allow us to distinguish between the BandCut and the simple Band model statistically if the break is above 100 MeV. On the other hand, cutoff features can be discerned more easily if there is an extra hard component (such as GRB 090926A and GRB 131108A), since the hard power-law component increases the number of the highest energy photons.

### 3.1. Compute the bulk Lorentz factor

If the spectral break/cutoff  $E_c$  is due to  $\gamma\gamma$  absorption within the source, one can compute the bulk Lorentz factor ( $\Gamma$ ) of the emitting region by taking  $\tau_{\gamma\gamma}(E_c) = 1$ . We consider a simple one-zone model where the photon field in the emitting region is uniform, isotropic and time independent in the comoving frame<sup>5</sup> (see the supporting material for Abdo et al. (2009b)). The target photons that annihilate with photons of energy  $E_c$  should have energy above  $E_t = \Gamma^2(m_e c^2)^2/[E_c(1+z)^2]$ , where  $z$  is the redshift. These photons come from the high energy part of the Band function or the extra power-law component, and their flux can be, respectively, parameterized as  $f(E) = f(E_0)(E/E_0)^\beta$  or  $f(E) = f(E_0)(E/E_0)^\lambda$  (in unit photons/(cm<sup>2</sup>keV)), where  $E_0$  is some reference energy. Considering that photons with energy  $E_c$  collide with target photons with energy above  $E_t$ , we get the  $\gamma\gamma$  absorption optical depth in the comoving frame Gould& Schröder (1967),

$$\tau_{\gamma\gamma}(E'_c) = \int_{-1}^1 d\mu' \int_{E'_t}^{E'_{max}} dE' n'_\gamma(E') \sigma_{\gamma\gamma}(E'_c, E', \mu') (1 - \mu') W' \quad (1)$$

where  $E'_c = (1+z)E_c/\Gamma$  (hereafter the prime represents quantities in the comoving frame),  $\sigma_{\gamma\gamma}$  is the absorption cross section,  $\mu' = \cos\theta'$ ,  $\theta'$  is the angle between the colliding photon pair,  $W'$  is the shell width, and  $E_{max}$  is the maximum energy of the target photons. Here  $n'_\gamma(E')$  is the number density of target photons in the comoving frame, which is given by Abdo et al. (2009b)

$$n'_\gamma(E') = \left(\frac{d_L}{R}\right)^2 \frac{\Gamma f(E_0)}{(1+z)^3 W'} \left(\frac{E'}{E_0}\right)^\beta, \quad (2)$$

where  $R$  is the radiation radius, and  $d_L$  is the luminosity distance. Introducing a dimensionless function  $F(\beta)$ , Abdo et al. (2009b) obtain a simplified expression of  $\tau_{\gamma\gamma}$ ,

$$\tau_{\gamma\gamma}(E'_c) = \sigma_T \left(\frac{d_L}{R}\right)^2 \frac{\Gamma E'_0 f(E_0)}{(1+z)^3} \left(\frac{E'_c E'_0}{m_e^2 c^4}\right)^{-\beta-1} F(\beta), \quad (3)$$

<sup>5</sup> Since cutoffs in our sample mostly occur at the high-energy part of the Band component, it is reasonable to consider the one-zone model, where high-energy photons come from the same region as the target photons. For the two-zone model, the calculation of the Lorentz factor would be different (Zou et al. 2011; Zhao et al. 2011).

where  $F(\beta) \approx 0.597(-\beta)^{-2.30}$  for  $-2.90 \leq \beta \leq -1.0$  (Abdo et al. 2009). The relation  $R \simeq \Gamma^2 c \delta t / (1+z)$  is valid for the internal shock model, where  $\delta t$  is the variability time. Setting  $\tau_{\gamma\gamma}(E_c) = 1$ , the Lorentz factor  $\Gamma$  is given by

$$\Gamma = \left[ \sigma_T \left( \frac{dL}{cdt} \right)^2 E_0 f(E_0) F(\beta) (1+z)^{-2(\beta+1)} \left( \frac{E_c E_0}{m_e^2 c^4} \right)^{-\beta-1} \right]^{1/(2(1-\beta))}. \quad (4)$$

One should note that Eq.(3) is obtained when the upper limit of the second integral in Eq.(1),  $E_{max}$ , is taken to be  $\infty$ , which is valid only when the energy of target photons that annihilate with  $E_c$  is well below the cutoff energy, i.e.,

$$E_c \gg \Gamma^2 m_e^2 c^4 / [E_c (1+z)^2] \quad (5)$$

(Li 2010; Zhao et al. 2011). This condition is usually satisfied when the cutoff energy  $E_c$  is larger than a few hundreds MeV. However, for bursts with lower  $E_c$ , such as some bursts in our sample, this condition is not satisfied anymore. For these low  $E_c$  bursts, the energy of target photons should be comparable to  $E_c$  (i.e.,  $E_c \gtrsim \Gamma^2 m_e^2 c^4 / [E_c (1+z)^2]$ ), then  $\Gamma$  is estimated to be (Li 2010)

$$\Gamma \approx \frac{E_c}{m_e c^2} (1+z). \quad (6)$$

Using the above method, we can now calculate  $\Gamma$  for each burst with spectral cutoffs. For GRB090926A, since the time-resolved spectra of the maximum spikes show spectral cutoffs, we use the cutoff energy for the time-resolved spectrum to calculate  $\Gamma$ . For 4 GRBs that do not have redshift measurements, we assume redshifts of  $z = 1$  for them. The variability time  $\delta t = 0.1$ s is adopted for GRB131108A, based on the 2 ms resolution lightcurve of the bright NaI detector. For GRB090926A,  $\delta t = 0.15$ s is adopted according to (Ackermann et al. 2011). We first use Eq. (4) to calculate  $\Gamma$ , and then check whether Eq.(5) is satisfied. We find that, only two bursts (GRB131108A and GRB090926A), which have relatively larger  $E_c$ , satisfy this condition. The other seven bursts all have  $E_c \lesssim 100$ MeV and Eq.5 is not satisfied for them, so their Lorentz factor  $\Gamma$  are calculated with Eq.(6). We note that this estimate of  $\Gamma$  suffers from less assumptions, as they are independent of the internal shock model assumption and the estimate of the variability timescale. The results of  $\Gamma$  are presented in Table 5. The values of  $\Gamma$  in our sample range from 90 to 900, providing direct evidence that GRBs are powered by ultra-relativistic outflow.

It has been usually suggested that, even if no spectral cutoff is measured, the observed highest energy photon can be used to place a lower limit on the bulk Lorentz factor, assuming that the absorption optical depth  $\tau_{\gamma\gamma}(E_{max}) \lesssim 1$  for the maximum energy photon (Krolik & Pier 1991; Fenimore et al. 1993; Woods & Loeb 1995; Baring & Harding 1997; Hascoët et al. 2012)). However, from our sample that have measured cutoffs, one can see that the absorption optical depth equals unity for the cutoff energy (i.e.  $\tau_{\gamma\gamma}(E_c) = 1$ ) and the absorption optical depth for the maximum energy photon is larger than unity (i.e.  $\tau_{\gamma\gamma}(E_{max}) > 1$ ). For this reason, the usual approach that uses  $\tau_{\gamma\gamma}(E_{max}) \lesssim 1$  for the highest energy photon to estimate the lower limits on the bulk Lorentz factors is inaccurate.

Another method for estimating the bulk Lorentz factors is from the peak in the early optical afterglow light curve, assuming that this peak is caused by the afterglow onset, at which the jet is decelerated (Sari & Piran 1999; Liang et al. 2010; Racusin et al. 2011; Hascoët et al. 2014). Although

most of the LAT bursts do not have early optical afterglow data, such estimate may be possible in some cases. The Lorentz factors can also be determined from the thermal component in the prompt emission, assuming it comes from the fireball photosphere (Pe'er et al. 2007). But this method depends on the unknown composition of GRBs outflow and the efficiency of dissipation mechanism responsible for the non-thermal component (Peng et al. 2014; Gao & Zhang 2014).

### 3.2. Correlations in $\Gamma - L_{\gamma,iso}$ and $\Gamma - E_{\gamma,iso}$

There have been suggestions that the Lorentz factors correlate with other quantities of the GRB jets, such as the isotropic gamma-ray luminosity or energy (Liang et al. 2010; Lü et al. 2012; Ghirlanda et al. 2012). The Lorentz factors in all the references are determined from the afterglow onset time, at which the jet is decelerated, so the values depends on the details of the dynamics and the circumburst environment. The Lorentz factors determined through the absorption cutoff in high-energy photons is more straightforward and reliable. We test the relation  $\Gamma - L_{\gamma,iso}$  and  $\Gamma - E_{\gamma,iso}$  using our sample, where  $L_{\gamma,iso}$  is the averaged, isotropic gamma-ray luminosity in 10-1000 keV and  $E_{\gamma,iso}$  is the isotropic gamma-ray energy in 10-1000 keV. The results are shown in Fig.2. We find the relation

$$\Gamma = 10^{1.65 \pm 0.20} L_{\gamma,iso,51}^{0.52 \pm 0.13}, \quad (7)$$

with a Pearson correlation coefficient of  $r = 0.844$  and null hypothesis probability of 0.008, which indicates a tight positive correlation. Removing the 4 GRBs that do not have redshift measurements, we examine whether the correlation remains. Although the sample gets smaller, we find that a correlation between  $\Gamma$  and  $L_{\gamma,iso}$  is still keep. Similarly, for the 8 GRBs, we find that

$$\Gamma = 10^{1.01 \pm 0.56} E_{\gamma,iso,52}^{0.88 \pm 0.35}, \quad (8)$$

with a Pearson correlation coefficient of  $r = 0.707$  and null hypothesis probability of 0.050. Although our results generally agree with earlier suggestions that more powerful GRBs move faster, the correlation slopes are different. We note that the number of GRBs in our sample is limited and the correlation remains to be tested with a large sample in future.

GRB jets are accelerated at the early stage while the internal energy of the fireball is gradually converted to the kinetic energy. After the acceleration, the jet is expected to have the Lorentz factor equal to the the initial dimensionless entropy  $\eta = L_0 / (\dot{M} c^2)$ , where  $L_0$  and  $\dot{M}$  are respectively the total energy and mass outflow rates. Considering the relation in Eq.7, the mass outflow rates should follow that  $\dot{M} \propto L_{\gamma,iso}^{0.48 \pm 0.13}$  (assuming that  $L_{\gamma,iso} \propto L_0$ ). This put useful constraint on any central engine models for GRBs.

### 3.3. Summary

We perform a complete analysis of the LAT-detected GRBs since August 2011, i.e. the bursts that are not included in the first *Fermi*/LAT GRB catalog (Ackermann et al. 2013). Our aim is to search for cutoff-like spectral feature in the high-energy gamma-ray emission, as has been seen in GRB 090926A. We find 6 GRBs showing such spectral features, with the cutoff energies ranging from  $\sim 10$  to  $\sim 500$  MeV. Assuming a simple one-zone model for the MeV-GeV emission, we compute the bulk Lorentz factors of the emitting region of these bursts. Motivated by earlier suggestion that the Lorentz factors may correlate with other burst quantities, such

as the isotropic gamma-ray luminosity or energy (Liang et al. 2010; Lü et al. 2012; Ghirlanda et al. 2012), we test these relations with our sample. It is found that the Lorentz factors are well correlated with the isotropic gamma-ray luminosity of the bursts, suggesting that more powerful GRB outflow move faster.

We thank the referee for the constructive report, and thank Zhuo Li, Xue-Feng Wu, and Hoi-Fung Yu for useful discussions. This work has made use of data and software provided by the Fermi Science Support Center. This work is supported by the 973 program under grant 2014CB845800, the NSFC under grants 11273016 and 11033002, and the Excellent Youth Foundation of Jiangsu Province (BK2012011). PHT is supported by the One Hundred Talents Program of the Sun Yat-Sen University.

## REFERENCES

- Abdo, A. A., Ackermann, M., Ajello, M., et al. 2009a, *ApJ*, 706, L138  
 Abdo, A. A., Ackermann, M., Arimoto, M., et al. 2009b, *Science*, 323, 1688  
 Ackermann, M., Asano, K., Atwood, W. B., et al. 2010, *ApJ*, 716, 1178  
 Ackermann, M., Ajello, M., Asano, K., et al. 2011, *ApJ*, 729, 114  
 Ackermann, M., Ajello, M., Asano, K., et al. 2013, *ApJS*, 209, 11  
 Ackermann, M., Ajello, M., Asano, K., et al. 2014, *Science*, 343, 42  
 Axelsson, M., Baldini, L., Barbiellini, G., et al. 2012, *ApJ*, 757, L131  
 Arimoto, M., & Bissaldi, E. 2014, *GRB Coordinates Network*, 16633, 1  
 Band, D., Matteson, J., Ford, L., et al. 1993, *ApJ*, 413, 281  
 Baring, M. G., & Harding, A. K. 1997, *ApJ*, 491, 663  
 Bissaldi, E., Desiante, R., Axelsson, M., Kocevski, & Piron, F. 2014, *GRB Coordinates Network*, 16623, 1  
 Bissaldi, E., Racusin, J., Longo, F., Kocevski, D., Vianello, G., & Arimoto, M. 2014, *GRB Coordinates Network*, 16969, 1  
 Bissaldi, E., Sonbas, E., Longo, F., & Racusin, J. 2014, *GRB Coordinates Network*, 15714, 1  
 Bissaldi, E., Vianello, G., & Chiang, J. 2014, *GRB Coordinates Network*, 16069, 1  
 Bissaldi, E., Vianello, G., Longo, F., Desiante, R., & Racusin, J. 2014, *GRB Coordinates Network*, 15791, 1  
 Burgess, J. M., Preece, R. D., Connaughton, V., et al. 2014, *ApJ*, 784, 17  
 Burgess, J. M., Preece, R. D., Baring, M. G., et al. 2011, *ApJ*, 741, 24  
 Burgess, J. M., Connaughton, V., & Xiong, S. 2013, *GRB Coordinates Network*, 14583, 1  
 Burns, E. 2014, *GRB Coordinates Network*, 16626, 1  
 Chaplin, V., & Fitzpatrick, G. 2013, *GRB Coordinates Network*, 14346, 1  
 Collazzi, A. C. 2013, *GRB Coordinates Network*, 15129, 1  
 Connaughton, V., Zhang, B.-B., Fitzpatrick, G., & Roberts, O. 2014, *GRB Coordinates Network*, 16419, 1  
 Cucchiara, A. 2014a, *GRB Coordinates Network*, 15652, 1  
 Cucchiara, A. 2014b, *GRB Coordinates Network*, 16982, 1  
 de Ugarte Postigo, A., Thoene, C. C., Gorosabel, J., et al. 2013, *GRB Coordinates Network*, 15470, 1  
 Desiante, R., Kocevski, D., Vianello, G., et al. 2013, *GRB Coordinates Network*, 15333, 1  
 Fenimore, E. E., Epstein, R. I., & Ho, C. 1993, *A&AS*, 97, 59  
 Fitzpatrick, G., & Xiong, S. 2013, *GRB Coordinates Network*, 15332, 1  
 Gao, H., & Zhang, B. 2014, arXiv:1409.3584  
 Ghirlanda, G., Nava, L., Ghisellini, G., et al. 2012, *MNRAS*, 420, 483  
 Giuliani, A., Mereghetti, S., Marisaldi, M., et al. 2014, arXiv:1407.0238  
 Goldstein, A., Burgess, J. M., Preece, R. D., et al. 2012, *ApJS*, 199, 19  
 Gould, R. J., & Schröder, G. P. 1967, *Physical Review*, 155, 1408  
 Gruber, D., Goldstein, A., Weller von Ahlefeld, V., et al. 2014, *ApJS*, 211, 12  
 Guiriec, S., Connaughton, V., & Briggs, M. 2012, *GRB Coordinates Network*, 13429, 1  
 Guiriec, S., Kouveliotou, C., Daigne, F., et al. 2015, arXiv:1501.07028  
 Guiriec, S., Daigne, F., Hascoët, R., et al. 2013, *ApJ*, 770, 32  
 Guiriec, S., Connaughton, V., Briggs, M. S., et al. 2011, *ApJ*, 727, L133  
 Hascoët, R., Beloborodov, A. M., Daigne, F., & Mochkovitch, R. 2014, *ApJ*, 782, 5  
 Hascoët, R., Daigne, F., Mochkovitch, R., & Vennin, V. 2012, *MNRAS*, 421, 525  
 Hurley, K. 2013, *GRB Coordinates Network*, 15467, 1  
 Jenke, P. 2013a, *GRB Coordinates Network*, 15113, 1  
 Jenke, P. 2013b, *GRB Coordinates Network*, 15261, 1  
 Jenke, P., & Xiong, S. 2014, *GRB Coordinates Network*, 15644, 1  
 Jenke, P. A., & Yu, H.-F. 2014, *GRB Coordinates Network*, 16070, 1  
 Kocevski, D., Longo, F., Vianello, G., et al. 2014, *GRB Coordinates Network*, 16420, 1  
 Kocevski, D., Ohno, M., Racusin, J., et al. 2013, *GRB Coordinates Network*, 14574, 1  
 Kocevski, D., Omodei, N., Racusin, J., et al. 2013, *GRB Coordinates Network*, 15115, 1  
 Kocevski, D., Vianello, G., & Chiang, J. 2012, *GRB Coordinates Network*, 13423, 1  
 Kocevski, D., Vianello, G., Chiang, J., & Racusin, J. 2013, *GRB Coordinates Network*, 14532, 1  
 Krolik, J. H., & Pier, E. A. 1991, *ApJ*, 373, 277  
 Lü, J., Zou, Y.-C., Lei, W.-H., et al. 2012, *ApJ*, 751, 49  
 Li, Z. 2010, *ApJ*, 709, 525  
 Liang, E.-W., Yi, S.-X., Zhang, J., et al. 2010, *ApJ*, 725, 2209  
 Lithwick, Y., & Sari, R. 2001, *ApJ*, 555, 540  
 McBreen, S. 2012, *GRB Coordinates Network*, 12826, 1  
 Ohno, M., McEnery, J., Vianello, G., Racusin, J. L., & Troja, E. 2013, *GRB Coordinates Network*, 14347, 1  
 Omodei, N., & McEnery, J. 2013, *GRB Coordinates Network*, 14675, 1  
 Paciasas, W. S., Meegan, C. A., von Kienlin, A., et al. 2012, *ApJS*, 199, 18  
 Pe'er, A., Ryde, F., Wijers, R. A. M. J., Mészáros, P., & Rees, M. J. 2007, *ApJ*, 664, L1  
 Pe'er, A., Zhang, B.-B., Ryde, F., et al. 2012, *MNRAS*, 420, 468  
 Pelassa, V. 2011, *American Institute of Physics Conference Series*, 1358, 41  
 Preece, R., Burgess, J. M., von Kienlin, A., et al. 2014, *Science*, 343, 51  
 Peng, F.-K., Liang, E.-W., Wang, X.-Y., et al. 2014, *ApJ*, 795, 155  
 Racusin, J. L., Vianello, G., Bissaldi, E., Desiante, R., & Longo, F. 2013, *GRB Coordinates Network*, 15399, 1  
 Racusin, J. L., Zhu, S., Kocevski, D., et al. 2013, *GRB Coordinates Network*, 15464, 1  
 Racusin, J. L., Oates, S. R., Schady, P., et al. 2011, *ApJ*, 738, 138  
 Roberts, O. J. 2014, *GRB Coordinates Network*, 16971, 1  
 Ryde, F., Pe'er, A., Nymark, T., et al. 2011, *MNRAS*, 415, 3693  
 Ryde, F., Axelsson, M., Zhang, B. B., et al. 2010, *ApJ*, 709, L172  
 Ryde, F., & Pe'er, A. 2009, *ApJ*, 702, 1211  
 Ryde, F. 2005, *ApJ*, 625, L95  
 Sari, R., & Piran, T. 1999, *ApJ*, 520, 641  
 Sonbas, E., Racusin, J. L., Kocevski, D., & McEnery, J. 2013, *GRB Coordinates Network*, 15640, 1  
 Sonbas, E., Vianello, G., & Longo, F. 2014, *GRB Coordinates Network*, 15659, 1  
 Stanbro, M. 2014, *GRB Coordinates Network*, 16636, 1  
 Tierney, D. 2012, *GRB Coordinates Network*, 13708, 1  
 Vasileiou, V. 2013, *Astroparticle Physics*, 48, 61  
 Vianello, G., Desiante, R., & Longo, F. 2013, *GRB Coordinates Network*, 15357, 1  
 Vianello, G., Longo, F., & Bissaldi, E. 2014, *GRB Coordinates Network*, 16034, 1  
 Vianello, G., McEnery, J., & Sonbas, E. 2014, *GRB Coordinates Network*, 15684, 1  
 Vianello, G., & Omodei, N. 2013, *GRB Coordinates Network*, 15587, 1  
 Vianello, G., Omodei, N., Racusin, J. L., & Jenke, P. 2012, *GRB Coordinates Network*, 13085, 1  
 Vianello, G., Racusin, J., & Arimoto, M. 2014, *GRB Coordinates Network*, 16322, 1  
 Vianello, G., Racusin, J., & Donato, D. 2012, *GRB Coordinates Network*, 13704, 1  
 Vianello, G., & Sonbas, E. 2013, *GRB Coordinates Network*, 15128, 1  
 von Kienlin, A. 2014, *GRB Coordinates Network*, 15790, 1  
 von Kienlin, A. 2013, *GRB Coordinates Network*, 14473, 1  
 von Kienlin, A., & Connaughton, V. 2014, *GRB Coordinates Network*, 15716, 1  
 von Kienlin, A., & Connaughton, V. 2014, *GRB Coordinates Network*, 16321, 1  
 von Kienlin, A., & Jenke, P. 2013, *GRB Coordinates Network*, 15401, 1  
 von Kienlin, A., & Meegan, C. 2013, *GRB Coordinates Network*, 15591, 1  
 von Kienlin, A., & Younes, G. 2013, *GRB Coordinates Network*, 14530, 1  
 von Kienlin, A., Meegan, C. A., Paciasas, W. S., et al. 2014, *ApJS*, 211, 13  
 Woods, E., & Loeb, A. 1995, *ApJ*, 453, 583  
 Xiong, S. 2014, *GRB Coordinates Network*, 15687, 1  
 Xiong, S. 2013, *GRB Coordinates Network*, 14674, 1

- Xu, D., Malesani, D., & Pursimo, T. 2013, GRB Coordinates Network, 15471, 1
- Xu, D., Levan, A. J., Fynbo, J. P. U., et al. 2014a, GRB Coordinates Network, 16983, 1
- Xu, D., Malesani, D., Tanvir, N. R., et al. 2014b, GRB Coordinates Network, 15645, 1
- Younes, G. 2013, GRB Coordinates Network, 15477, 1
- Yu, H.-F., & von Kienlin, A. 2014, GRB Coordinates Network, 16032, 1
- Yu, H.-F., Greiner, J., van Eerten, H., et al. 2015, A&A, 573, AA81
- Zhang, B.-B. 2013, GRB Coordinates Network, 15360, 1
- Zhang, B.-B., & Bhat, N. 2014, GRB Coordinates Network, 15669, 1
- Zhao, X.-H., Li, Z., & Bai, J.-M. 2011, ApJ, 726, 89
- Zheng, W., & Akerlof, C. 2012, GRB Coordinates Network, 12822, 1
- Zhu, S., Racusin, J., Chiang, J., & Vianello, G. 2013, GRB Coordinates Network, 14508, 1
- Zou, Y.-C., Fan, Y.-Z., & Piran, T. 2011, ApJ, 726, LL2

**Table 1**  
Properties of *Fermi*/LAT GRBs from Aug 2011 to Oct 2014

GRB name	Class <sup>a</sup>	T <sub>90</sub> <sup>b</sup> (s)	T <sub>90</sub> <sup>S b</sup> (s)	$\theta^c$ (deg)	RA <sup>d</sup> (deg)	Decl. <sup>d</sup> (deg)	LLE&GBM <sup>e</sup>	Ref <sup>f</sup>
120107A	L	23.04	0.064	56	246.4	-69.93	b0,n6,n7	1
120316A	L	26.624	1.536	9	57.97	-56.46	LLE,b0,n0,n1	2
120709A	L	27.328	-0.128	22	318.41	-50.03	LLE,b1,n6,n7,n9	3
120830A	S	1.28	-0.384	38	88.42	28.81	b0,n0,n1,n3	4
130327B	L	31.233	2.048	47	218.09	-69.51	b0,n0,n1	5
130427A	L	138.242	4.096	48	173.15	27.71	LLE,b1,n9,n10	6
130502B	L	24.32	7.168	47	66.65	71.08	b1,n6,n7	7
130504C	L	73.217	8.704	47	91.72	3.85	LLE,b0,n2,n9	8
130518A	L	48.577	9.92	43	355.81	47.64	LLE,b1,n3,n7	9
130821A	L	87.041	3.584	37	314.1	-12	LLE,b1,n6,n9	10
130828A	L	136.45	13.312	40	259.83	28	b0,n0,n3	11
131014A	L	3.2	0.96	71.9	100.5	-19.1	LLE,b1,n9,na,nb	12
131018B	L	39.936	-1.024	12	304.41	23.11	b1,n6,n7	13
131029A	L	104.449	1.024	6	200.79	48.3	b0,n3,n5	14
131108A	L	18.496	0.448	27	156.47	9.9	LLE,b1,n3,n6	15
131209A	L	13.568	2.816	20	136.5	-33.2	b1,n6,n7	16
131231A	L	31.232	13.312	40	10.59	-1.85	LLE,b0,n0,n3	17
140102A	L	3.648	0.448	47	211.88	1.36	LLE,b1,n6,n7,n9,nb	18
140104B	L	188.417	9.216	25	218.81	-8.9	b1,n6,n7	19
140110A	L	9.472	-0.256	30	28.9	-36.26	LLE,b1,n6,n7,n9	20
140206B	L	116.738	8.256	45	315.26	-8.51	LLE,b0,n0,n1,n3	21
140323A	L	111.426	5.056	31	356.46	-79.87	b0,n0,n1	22
140402A	S	0.32	-0.128	13	207.47	5.87	b0,n1,n3	23
140523A	L	19.2	0.576	60	133.3	24.95	b0,n3,n4	24
140619B	S	2.816	-0.256	32	132.68	-9.66	LLE,b1,n6,n9	25
140723A	L	56.32	0	55	210.63	-3.73	b1,n9,na	26
140729A	L	55.553	0.512	26.2	193.95	15.35	LLE,b1,n6,n8,n9	27
141028A	L	31.489	6.656	25	322.7	-0.28	LLE,b1,n6,n7,n9	28
090926A	L	13.76	2.176	48.1	353.4	-66.32	LLE,b1,n3,n6,n7	29
100724B	L	114.69	8.192	48.9	119.89	76.55	LLE,b0,n0,n1	29

<sup>a</sup> L means long burst and S means short burst.

<sup>b</sup> GBM T90 duration and the start time from GBM trigger time cited from GBM catalog, i.e., Paciesas et al. (2012); Goldstein et al. (2012); Gruber et al. (2014); von Kienlin et al. (2014).

<sup>c</sup> Off-axis angle at the trigger time derived from reference in the ninth collum.

<sup>d</sup> LAT position from reference in the ninth collum.

<sup>e</sup> LLE represents the publicly LAT Low-Energy data; others are the GBM detectors we used for spectral analysis.

<sup>f</sup> **Reference:** 1: Zheng, W. & Akerlof, C. (2012); McBreen, S. (2012); 2: Vianello, G. et al. (2012); 3: Kocevski, D. et al. (2012); Guiriec, S. et al. (2012); 4: Vianello, G. et al. (2012); Tierney, D. (2012); 5: Ohno, M. et al. (2013); Chaplin, V. & Fitzpatrick, G. (2013); 6: Zhu, S. et al. (2013); von Kienlin, A. (2013); 7: Kocevski, D. et al. (2012); von Kienlin, A. & Younes, G. (2013); 8: Kocevski, D. et al. (2013); Burgess, J. M. et al. (2013); 9: Omodei, N. & McEnery, J. (2013); Xiong, S. (2013); 10: Kocevski, D. et al. (2013); Jenke, P. (2013b); 11: Vianello, G. & Sonbas, E. (2013); Collazzi, A. C. (2013); 12: Desiante, R. et al. (2013); Fitzpatrick, G. & Xiong, S. (2013); 13: Vianello, G. et al. (2013); Zhang, B.-B. (2013); 14: Racusin, J. L. et al. (2013); von Kienlin, A. & Jenke, P. (2013); 15: Racusin, J. L. et al. (2013); Younes, G. (2013); 16: Vianello, G. & Omodei, N. (2013); von Kienlin, A. & Meegan, C. (2013); 17: Sonbas, E. et al. (2013); Jenke, P. & Xiong, S. (2014); 18: Sonbas, E. et al. (2014); Zhang, B.-B. & Bhat, N. (2014); 19: Vianello, G. et al. (2014); Xiong, S. (2014); 20: Bissaldi, E. et al. (2014); von Kienlin, A. & Connaughton, V. (2014); 21: Bissaldi, E. et al. (2014); von Kienlin, A. (2014); 22: Vianello, G. et al. (2014); Yu, H.-F. & von Kienlin, A. (2014); 23: Bissaldi, E. et al. (2014); Jenke, P. A. & Yu, H.-F. (2014); 24: Vianello, G. et al. (2014); von Kienlin, A. & Connaughton, V. (2014); 25: Kocevski, D. et al. (2014); Connaughton, V. et al. (2014); 26: Bissaldi, E. et al. (2014); Burns, E. (2014); 27: Arimoto, M. & Bissaldi, E. (2014); Stanbro, M. (2014); 28: Bissaldi, E. et al. (2014); Roberts, O. J. (2014). 29: Ackermann et al. (2013)

**Table 2**  
Joint spectral fits of the sample modelled by the Band function

GRB name	model	$\alpha$	$\beta$	$E_p(\text{keV})$	CSTAT/DOF
120107A	Band	$-1.19 \pm 0.08$	$-2.39 \pm 0.11$	$275.2 \pm 59.7$	396/381
120316A	Band	$-0.74 \pm 0.03$	$-2.71 \pm 0.11$	$421.4 \pm 14.4$	17216/383
120709A	Band	$-1.06 \pm 0.04$	$-2.59 \pm 0.07$	$423.1 \pm 39.2$	715/510
120830A	Band	$-0.13 \pm 0.11$	$-2.63 \pm 0.11$	$887.7 \pm 103.0$	576.9/505
130327B	Band	$-0.64 \pm 0.02$	$-2.74 \pm 0.09$	$327 \pm 8.2$	607.7/383
130427A	Band+PL	$-0.87 \pm 0.01$	$-2.83 \pm 0.01$	$900.1 \pm 7.0$	1146/370
130502B	Band	$-0.51 \pm 0.01$	$-2.61 \pm 0.03$	$280.6 \pm 3.6$	594/370
130518A	Band	$-0.89 \pm 0.01$	$-2.72 \pm 0.04$	$400 \pm 10.3$	676.8/385
130828A	Band	$-1.12 \pm 0.11$	$-2.45 \pm 0.06$	$243.5 \pm 21.7$	549/326
131014A	Band	$-0.21 \pm 0.01$	$-2.62 \pm 0.02$	$308.5 \pm 2.7$	990/487
131018B	Band	$-0.20 \pm 0.41$	$-3.77 \pm 2.61$	$77.7 \pm 10.8$	608.2/381
131029A	Band	$-0.98 \pm 0.05$	$-2.32 \pm 0.05$	$230.2 \pm 20.6$	575/381
131209A	Band	$-0.34 \pm 0.05$	$-2.97 \pm 0.36$	$281.3 \pm 13.9$	401/381
140102A	Band	$-0.75 \pm 0.02$	$-2.58 \pm 0.04$	$182.1 \pm 4.3$	808/632
140104B <sup>a</sup>	Band	$-0.68 \pm 0.16$	$-3.00(\text{fixed})$	$218.8 \pm 14.7$	840.9/324
140110A	Band	$-0.72 \pm 0.06$	$-2.53 \pm 0.07$	$1431 \pm 266$	900/511
140323A	Band	$-0.99 \pm 0.03$	$-2.41 \pm 0.06$	$143.2 \pm 6.8$	3185/383
140402A	Band	$0.49 \pm 0.62$	$-2.28 \pm 0.1$	$715.2 \pm 202$	397/382
140523A	Band	$-0.94 \pm 0.01$	$-2.62 \pm 0.06$	$243.2 \pm 5.8$	549/380
140619B	Band	$-0.28 \pm 0.32$	$-2.14 \pm 0.05$	$680.6 \pm 215$	419/397
140723A	Band	$-1.14 \pm 0.05$	$-2.34 \pm 0.07$	$1383 \pm 460$	822.1/380
140729A	Band	$-0.86 \pm 0.06$	$-2.74 \pm 0.11$	$929.4 \pm 155$	1813/504

<sup>a</sup> In this fit, the energy range of NaI starts from  $>\sim 50$  keV.

**Table 3**  
Joint spectral fits for the sample with high energy cutoffs

GRB name	model	$\alpha$	$\beta$	$E_p(\text{keV})$	$\lambda$	$E_c(\text{MeV})$	CSTAT/DOF	$\Delta\text{CSTAT}$
090926A	Band+PLCut	$-0.50 \pm 0.03$	$-2.54 \pm 0.03$	$269.8 \pm 3.7$	$-1.78 \pm 0.02$	$550.2 \pm 91.5$	983.1/486	135.8
...	Band	$-0.71 \pm 0.01$	$-2.31 \pm 0.01$	$285.3 \pm 3.2$	—	—	1118.9/489	—
100724B	BandCut	$-0.71 \pm 0.01$	$-2.08 \pm 0.01$	$354.5 \pm 1.5$	—	$42.4 \pm 4.0$	1202.3/389	342.8
...	Band	$-0.77 \pm 0.01$	$-2.43 \pm 0.01$	$417.9 \pm 6.6$	—	—	1545.1/390	—
130504C	BandCut	$-1.21 \pm 0.01$	$-2.03 \pm 0.01$	$619.6 \pm 7.8$	—	$22.2 \pm 6.3$	740.3/389	70.2
...	Band	$-1.23 \pm 0.01$	$-2.66 \pm 0.03$	$722.1 \pm 30.7$	—	—	810.5/390	—
130821A	BandCut	$-1.04 \pm 0.01$	$-2.12 \pm 0.02$	$297.6 \pm 2.9$	—	$13.3 \pm 7.3$	793.7/388	40.7
...	Band	$-1.08 \pm 0.01$	$-2.78 \pm 0.05$	$341.9 \pm 10.8$	—	—	834.4/389	—
131108A	Band+PLCut	$-0.69 \pm 0.09$	$-2.59 \pm 0.16$	$291.5 \pm 15.8$	$-1.69 \pm 0.04$	$347.1 \pm 52.8$	411.4/385	29.5
...	Band	$-0.88 \pm 0.03$	$-2.16 \pm 0.01$	$308.5 \pm 14.6$	—	—	440.9/388	—
131231A	BandCut	$-1.21 \pm 0.01$	$-2.43 \pm 0.01$	$205.9 \pm 0.8$	—	$61.6 \pm 22.5$	1175.8/380	31
...	Band	$-1.22 \pm 0.01$	$-2.62 \pm 0.02$	$214.3 \pm 3.1$	—	—	1206.8/381	—
140206B	BandCut	$-1.14 \pm 0.01$	$-2.03 \pm 0.01$	$241.2 \pm 1.9$	—	$50.1 \pm 6.8$	2392.0/511	108.4
...	Band	$-1.17 \pm 0.01$	$-2.34 \pm 0.01$	$276.6 \pm 7.4$	—	—	2500.4/512	—
141028A	BandCut	$-0.83 \pm 0.01$	$-2.05 \pm 0.01$	$288.6 \pm 2.9$	—	$53.2 \pm 7.3$	1101.3/510	92.8
...	Band	$-0.86 \pm 0.02$	$-2.37 \pm 0.02$	$316.3 \pm 11.7$	—	—	1194.1/511	—
090926A-a	Band+PLCut	$-0.91 \pm 0.09$	$-2.66 \pm 0.37$	$226.2 \pm 9.2$	$-1.69 \pm 0.03$	$350.7 \pm 41.3$	492.4/479	68.1
...	Band	$-1.01 \pm 0.03$	$-2.12 \pm 0.01$	$231.4 \pm 10.1$	—	—	560.5/482	—

**Note.** — The top panel are the results for the time-integrated spectra. The bottom panel are the results for the time-resolved spectra of GRB 090926A in the interval of [9.79s, 10.50s].

**Table 4**  
Burst parameters and the derived Lorentz factor of GRBs

GRB name	$E_c(\text{MeV})$	$z^a$	$L_{\gamma,iso}^b$	$E_{\gamma,iso}^c$	$\Gamma^d$	$z$ Ref <sup>e</sup>
100724B	$42.4 \pm 4$	—	$10.1 \pm 0.1$	$58.2 \pm 0.6$	$165.9 \pm 15.6$	—
130504C	$22.2 \pm 6.3$	—	$8.9 \pm 0.1$	$32.7 \pm 0.3$	$86.7 \pm 24.5$	—
130821A	$13.3 \pm 7.3$	—	$7.1 \pm 0.1$	$18.4 \pm 0.3$	$52.1 \pm 28.6$	—
131231A	$61.6 \pm 22.5$	0.642	$8.7 \pm 0.1$	$16.5 \pm 0.1$	$197.9 \pm 72.3$	(1)
140206B	$50.1 \pm 6.8$	—	$5.2 \pm 0.1$	$30.2 \pm 0.4$	$196.1 \pm 26.6$	—
141028A	$53.2 \pm 7.3$	2.332	$57.7 \pm 1.3$	$54.5 \pm 1.2$	$346.9 \pm 47.6$	(2)
131108A	$347.1 \pm 52.8$	2.4	$90.7 \pm 1.2$	$49.4 \pm 0.7$	$734.4 \pm 111.7$	(3)
090926A	$350.7 \pm 41.3$	2.1	$365.1 \pm 13.7$	$215.1 \pm 8.1$	$748.3 \pm 88.1$	(4)

<sup>a</sup> Redshifts of GRBs. Bursts with no redshift measurements are assumed to have  $z = 1$ .

<sup>b</sup> Isotropic gamma-ray luminosity in 10-1000 keV obtained from the best fit of each GRB in unit of  $10^{50}$  erg  $s^{-1}$ .

<sup>c</sup> Isotropic gamma-ray energy in 10-1000 keV obtained from the best fit of each GRB in unit of  $10^{52}$  erg.

<sup>d</sup> The bulk Lorentz factor.

<sup>e</sup> (1) Xu, D. et al. (2014b), Cucchiara, A. (2014a); (2) de Ugarte Postigo, A. et al. (2013), Xu, D. et al. (2013); (3) Xu, D. et al. (2014a); (4) Ackermann et al.(2011).

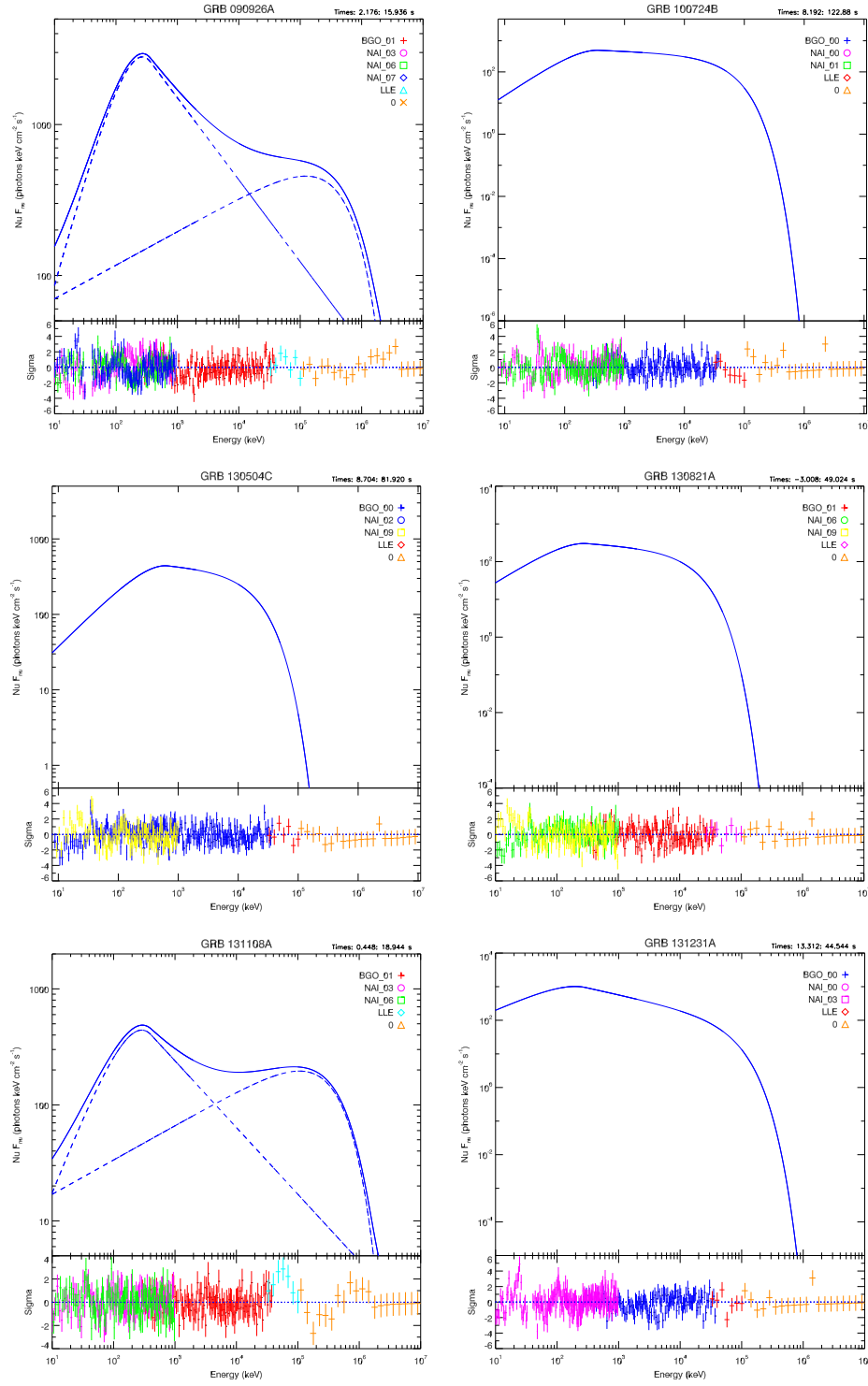


**Figure 1.** Spectral fits and residuals of the time integrated emission and the best-fit model of 8 GRBs showing high energy cutoffs. The top panels show  $\nu F_{\nu}$  spectra and the bottom panels show the residuals of the fit. The "O" represents the LAT data.

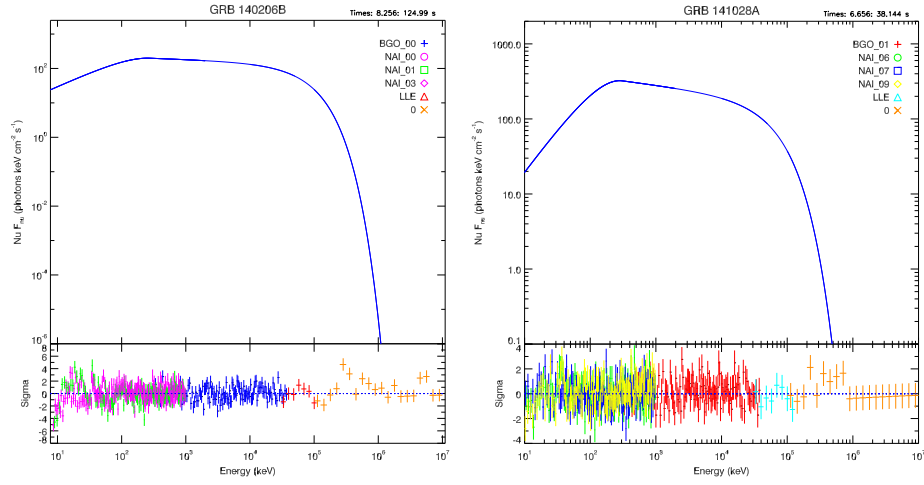
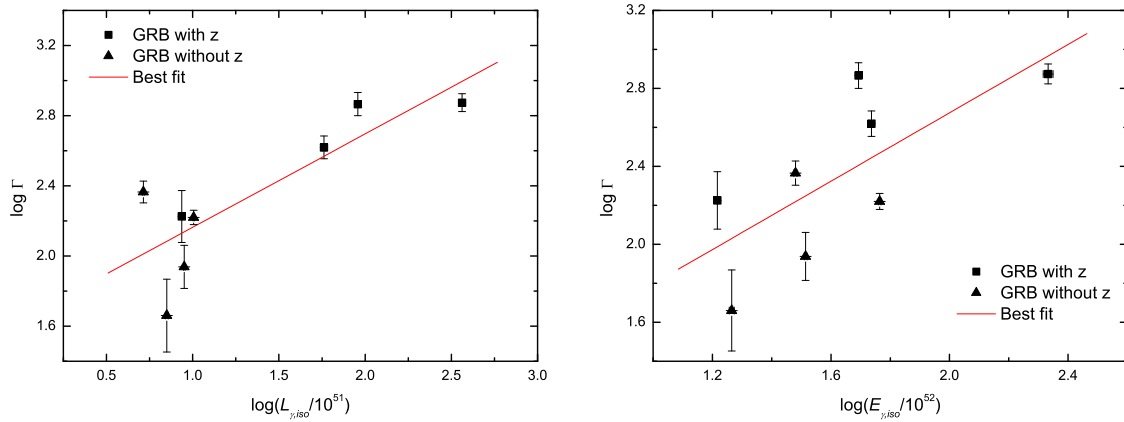


Figure 1. –continued



**Figure 2.** The bulk Lorentz factors as a function of the isotropic gamma-ray luminosity (top panel) or isotropic gamma-ray energy (bottom panel) for 8 bursts with detections of high-energy spectral cutoffs. GRBs with redshift measurements are marked with squares and those without redshift measurements are marked with triangles.